Temperature-drift effect analysis of microstrip filters based on parallel high-order DGTD and FETD method with memory reduction technique

Zhenglang Jia [a], Huanhuan Zhang [a],[*], Panpan Wang [a], Wei E.I. Sha [b]

[a] *National Key Laboratory of Antennas and Microwave Technology, Xidian University, Xian 710071, China*
[b] *College of Information Science and Electronic Engineering, Zhejiang University, Hangzhou 310058, China*

ARTICLE INFO

ABSTRACT

The temperature-drift effect of microstrip filters is analyzed by the proposed electromagnetic-thermal co-simulation method based on parallel high-order discontinuous Galerkin time domain (DGTD) and finite-element time-domain (FETD) algorithms with a memory reduction technique. The element matrices of DGTD method are factorized into the product of coefficient matrices and universal matrices. The coefficient matrices are different for each tetrahedral element and need to be stored for all the elements. While the universal matrices are the same for all the tetrahedral elements and only need to be stored for one element. Since the sizes of the coefficient matrices are much smaller than the element matrices of DGTD method, the proposed method avoids storing the large element matrices and greatly reduce the memory requirement of the DGTD method. Thus it reduces the memory requirement of the whole electromagnetic-thermal co-simulation which is dominated by the memory consumption of the DGTD method. Large-scale parallel technique is adopted to accelerate the process of electromagnetic-thermal co-simulation. The proposed method provides a very powerful tool for temperature-drift effect analysis of microstrip filters.

1. Introduction

Due to its advantages of small size, light weight, easy manufacture and low cost, the microstrip filters play a vital role in RF/microwave applications [1]. With the rapid development of wireless communications, electromagnetic spectrum resources are increasingly occupied. As a consequence, the guard band between two adjacent working frequency bands becomes extremely narrow, leading to a demand of high-performance microstrip filters. In order to make the wireless communication system work properly, the microstrip filters should have small passband insertion loss and fluctuation and large stopband attenuation. Moreover, the microstrip filters should withstand high input power and have good thermal stability.

The temperature characteristic of a microstrip filter is an important parameter to measure its performance. On the one hand, the temperature of a microstrip filter may increase greatly due to its power dissipation induced by high input power. On the other hand, the microstrip filter may operate under extreme environment, which can also greatly influence the temperature of the microstrip filter. If the microstrip filter is very sensitive to the temperature, its electromagnetic performances like insertion loss of passband and the stopband attenuation will change greatly with temperature variation. Therefore, the

temperature-drift effect analysis of microstrip filters is necessary and significant.

Since the temperature-drift effect of a microstrip filter involves both electromagnetic and thermal physics, electromagnetic-thermal co-simulation needs to be carried out to analyze this effect. Numerical methods like finite-difference time-domain (FDTD) method and finite element method (FEM) are usually adopted to solve Maxwell equation and heat conduction equation to implement the electromagnetic-thermal co-simulation [2–12]. For instance, the microwave heating problem is analyzed with the FDTD method in [2–4]. The electrothermal characteristics of power distribution networks, through-silicon-via (TSV) structures, and interconnects of the integrated circuits are simulated by the FEM method in [5–8]. The influence of the thermal effect on the electromagnetic performance of high-power microwave components is evaluated with FEM method in [9]. The temperature increase of human body induced by the electromagnetic radiation of cell phone is investigated with the FEM method in [10].

Recently, the discontinuous Galerkin time domain (DGTD) method is introduced into the electromagnetic-thermal co-simulation [11,12]. The DGTD method inherits the advantages of both the FDTD method and FEM method. It can use tetrahedron elements to accurately model the structures with curved surfaces, adopt higher-order basis functions

---

* Corresponding author.
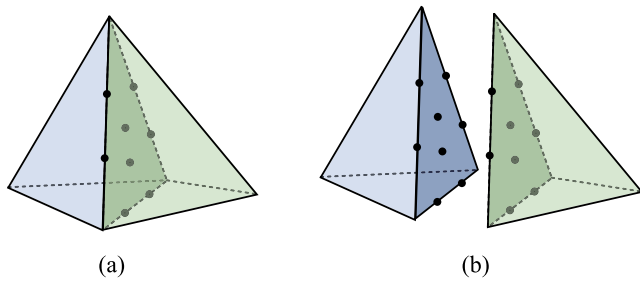*E-mail address:* hhzhang@xidian.edu.cn (H. Zhang).

Fig. 1. The unknowns on the common face of two adjacent elements in (a) FEM method and (b) DGTD method. Each dot represents an unknown.
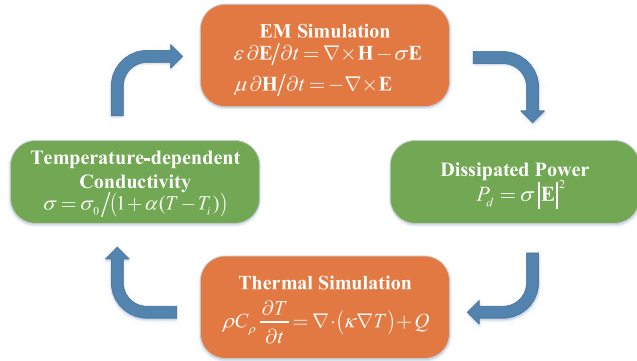

Fig. 2. Principle diagram of electromagnetic-thermal co-simulation.

to improve accuracy, avoid solving large global sparse matrix equation, naturally be combined with the parallel technique, etc. However, it must be pointed out that the DGTD method also has a serious shortcoming, namely high memory consumption. As shown in Fig. 1, the unknowns on the common face of two adjacent elements are the same in FEM method, while they are different in the DGTD method, which will make the number of unknowns on the common face double. Actually, if one edge is shared by multiple elements, the unknowns on the edge are different in all these elements, which greatly increases the total number of unknowns of DGTD method. As a result, the memory requirement of the DGTD method for the storage of matrix elements is much larger than the FEM method. For some complex and multiscale microstrip filter geometries, the total number of elements after spatial discretization will be huge, which makes the traditional DGTD based electromagnetic-thermal co-simulation unavailable for such a kind of problem. Here a memory reduction technique is utilized to reduce the memory cost of the high-order DGTD and FETD based electromagnetic-thermal co-simulation. Large-scale parallel technique is introduced to accelerate the simulation process. The proposed method provides a very powerful tool for temperature-drift effect analysis of microstrip filters.

2. Theories and formulations

2.1. General method for electromagnetic-thermal co-simulation

Fig. 2 shows the principle diagram of electromagnetic-thermal co-simulation. Firstly, the electromagnetic simulation is conducted with the governing equation of time-domain Maxwell curl equations:

$$\varepsilon \frac{\partial \mathbf{E}}{\partial t} = \nabla \times \mathbf{H} - \sigma \mathbf{E} \tag{1}$$

$$\mu \frac{\partial \mathbf{H}}{\partial t} = -\nabla \times \mathbf{E} \tag{2}$$

with the permittivity ε, permeability μ and conductivity σ.

These two equations are solved by the DGTD method to obtain the transient electric field $\mathbf{E}(\mathbf{r}, t_n)$ and magnetic field $\mathbf{H}(\mathbf{r}, t_n)$ at each time step t_n [13].

Then the dissipated power in the solution domain at t_n is calculated:

$$P_d = \sigma |\mathbf{E}|^2 \tag{3}$$

which serves as the transient heat source $Q(t_n)$ for thermal simulation.

After that, the thermal simulation is carried out with the governing equation of heat conduction equation:

$$\rho C_\rho \frac{\partial T}{\partial t} = \nabla \cdot (\kappa \nabla T) + Q \tag{4}$$

where ρ represents the mass density, C_ρ is the specific heat capacity, and κ refers to the thermal conductivity. This equation is solved by the FETD method to obtain the transient temperature distribution $T(\mathbf{r}, t_n)$ at t_n [14].

The modification of temperature has an influence on the constitutive parameters of materials like permittivities, permeabilities and conductivities in Maxwell curl equations. Here we only consider the temperature dependent conductivities for the sake of simplicity:

$$\sigma = \frac{\sigma_0}{1 + \alpha(T - T_i)} \tag{5}$$

where σ_0 represents the conductivity at initial temperature T_i, and α is the temperature coefficient of the material.

The changes of the constitutive parameters of materials will affect the distribution of electromagnetic fields. Thus the electromagnetic simulation at the next time step will be carried out again with the updated constitutive parameters of materials. This process repeats until the predetermined number of time steps N_t is completed or steady solution is reached.

The reason why we do not adopt the DGTD method for thermal simulation is given as follows. (1) The heat conduction equation is a parabolic partial differential equation. Contrarily, the DGTD method can only be applied to hyperbolic partial differential equations. In order to use the DGTD for the thermal simulation, an auxiliary vector variable needs to be introduced to transform the heat conduction equation to a hyperbolic equation [15,16], which makes a simple problem complicated. Moreover, the memory requirement will increase greatly if the DGTD method is utilized for the thermal simulation. (2) According to [15], only Dirichlet boundary condition and convection boundary condition were implemented for the thermal simulation. However, the thermal radiation boundary condition cannot be implemented since the contained nonlinear terms in radiation boundary condition cannot be expressed in the numerical fluxes of the DGTD method. The thermal radiation boundary condition is indispensable since any object above the absolute zero will emit heat to environment. It is convenient to implement the thermal radiation boundary condition in FETD method [14].

2.2. Memory reduction of DGTD method for electromagnetic-thermal co-simulation

As described in Section 1, the memory consumption of the DGTD method is higher than the FEM method. Therefore, the memory cost of the DGTD method for electromagnetic simulation is much more than that of the FETD method for thermal simulation. To alleviate this computational issue, a memory reduction technique is introduced to the DGTD method to reduce the memory cost of the electromagnetic-thermal co-simulation.

The final full-discrete marching-on-in-time matrix equation for the DGTD method with an upwind numerical flux can be expressed as [13]:

$$\mathbf{e}_{n+1}^i = \mathbf{e}_n^i + (\Delta t / \varepsilon) \left[\mathbf{M}^i \right]^{-1} \left[\mathbf{S}^i \mathbf{h}_{n+1/2}^i + \mathbf{F}_{ee}^{ii} \mathbf{e}_n^i - \mathbf{F}_{ee}^{ij} \mathbf{e}_n^j - \mathbf{F}_{eh}^{ii} \mathbf{h}_{n+1/2}^i \right.$$
$$\left. + \mathbf{F}_{eh}^{ij} \mathbf{h}_{n+1/2}^j - \mathbf{C}^i \mathbf{e}_n^i \right] \tag{6}$$

Table 1
The expansion coefficients N_{km} of the twenty second order hierarchical vector basis functions.

k	m		
	1	2	3
1	$-L_2$	L_1	0
2	$-L_3$	0	L_1
3	$-1 + L_2 + L_3$	$-L_1$	$-L_1$
4	0	$-L_3$	L_2
5	L_2	$1 - L_1 - L_3$	L_2
6	$-L_3$	$-L_3$	$-1 + L_1 + L_2$
7	L_2	L_1	0
8	L_3	0	L_1
9	$1 - 2L_1 - L_2 - L_3$	$-L_1$	$-L_1$
10	0	L_3	L_2
11	$-L_2$	$1 - L_1 - 2L_2 - L_3$	$-L_2$
12	$-L_3$	$-L_3$	$1 - L_1 - L_2 - 2L_3$
13	$-L_2 L_3$	$L_1 L_3$	0
14	$-L_3(1 - L_1 - L_2 - L_3)$	0	$L_1(1 - L_1 - L_2 - L_3)$
15	$-L_2(1 - L_1 - L_2 - L_3)$	$L_1(1 - L_1 - L_2 - L_3)$	0
16	0	$-L_3(1 - L_1 - L_2 - L_3)$	$L_2(1 - L_1 - L_2 - L_3)$
17	0	$L_1 L_3$	$-L_1 L_2$
18	$L_1 L_3$	$L_1 L_3$	$L_1(1 - L_1 - L_2)$
19	$L_1 L_2$	$L_1(1 - L_1 - L_3)$	$L_1 L_2$
20	$L_2 L_3$	$L_2 L_3$	$L_2(1 - L_1 - L_2)$

Fig. 3. (a) Tetrahedral element in a global (x, y, z)-coordinate system (b) Tetrahedral element in a normalized (L_1, L_2, L_3)-coordinate system.

$$\mathbf{h}_{n+3/2}^i = \mathbf{h}_{n+1/2}^i + (\Delta t/\mu) \left[\mathbf{M}^i\right]^{-1} \left[-\mathbf{S}^i \mathbf{e}_{n+1}^i + \mathbf{F}_{hh}^{ii} \mathbf{h}_{n+1/2}^i - \mathbf{F}_{hh}^{ij} \mathbf{h}_{n+1/2}^j \right.$$
$$\left. + \mathbf{F}_{he}^{ii} \mathbf{e}_{n+1}^i - \mathbf{F}_{he}^{ij} \mathbf{e}_{n+1}^j \right] \tag{7}$$

where

$$\left[\mathbf{M}^i\right]_{kl} = \int_{V_i} \mathbf{N}_k^i \cdot \mathbf{N}_l^i dV \tag{8}$$

$$\left[\mathbf{S}^i\right]_{kl} = \int_{V_i} \mathbf{N}_k^i \cdot (\nabla \times \mathbf{N}_l^i) dV \tag{9}$$

$$\left[\mathbf{F}_{eh}^{ii}\right]_{kl} = \frac{Z^j}{Z^i + Z^j} \int_{\partial V_i} \mathbf{N}_k^i \cdot (\hat{n} \times \mathbf{N}_l^i) dS \tag{10}$$

$$\left[\mathbf{F}_{eh}^{ij}\right]_{kl} = \frac{Z^j}{Z^i + Z^j} \int_{\partial V_i} \mathbf{N}_k^i \cdot (\hat{n} \times \mathbf{N}_l^j) dS \tag{11}$$

$$\left[\mathbf{F}_{he}^{ii}\right]_{kl} = \frac{Y^j}{Y^i + Y^j} \int_{\partial V_i} \mathbf{N}_k^i \cdot (\hat{n} \times \mathbf{N}_l^i) dS \tag{12}$$

$$\left[\mathbf{F}_{he}^{ij}\right]_{kl} = \frac{Y^j}{Y^i + Y^j} \int_{\partial V_i} \mathbf{N}_k^i \cdot (\hat{n} \times \mathbf{N}_l^j) dS \tag{13}$$

$$\left[\mathbf{F}_{ee}^{ii}\right]_{kl} = \frac{1}{Z^i + Z^j} \int_{\partial V_i} \mathbf{N}_k^i \cdot (\hat{n} \times \hat{n} \times \mathbf{N}_l^i) dS \tag{14}$$

$$\left[\mathbf{F}_{ee}^{ij}\right]_{kl} = \frac{1}{Z^i + Z^j} \int_{\partial V_i} \mathbf{N}_k^i \cdot (\hat{n} \times \hat{n} \times \mathbf{N}_l^j) dS \tag{15}$$

$$\left[\mathbf{F}_{hh}^{ii}\right]_{kl} = \frac{1}{Y^i + Y^j} \int_{\partial V_i} \mathbf{N}_k^i \cdot (\hat{n} \times \hat{n} \times \mathbf{N}_l^i) dS \tag{16}$$

$$\left[\mathbf{F}_{hh}^{ij}\right]_{kl} = \frac{1}{Y^i + Y^j} \int_{\partial V_i} \mathbf{N}_k^i \cdot (\hat{n} \times \hat{n} \times \mathbf{N}_l^j) dS \tag{17}$$

$$\left[\mathbf{C}^i\right]_{kl} = \int_{V_i} \sigma \mathbf{N}_k^i \cdot \mathbf{N}_l^i dV \tag{18}$$

The superscript i or j means that the quantity relates to the ith element or adjacent jth element. N_k is the basis function. The second-order hierarchical vector basis functions are adopted [17,18]:

$$\mathbf{N}_k = \sum_{m=1}^{3} N_{km} (L_1, L_2, L_3) \nabla L_m \quad k = 1, \ldots, 20 \tag{19}$$

where $L_m (m = 1, 2, 3, 4)$ is the volume coordinate of the tetrahedron element and $L_1 + L_2 + L_3 + L_4 = 1$. The expansion coefficients $N_{km} (L_1, L_2, L_3)$ are given in Table 1. Since the total number of the
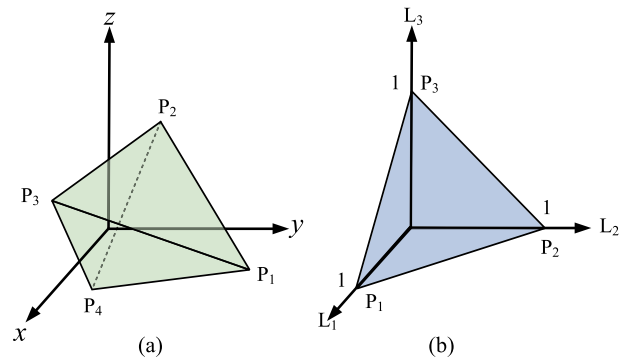
second-order hierarchical vector basis functions is twenty in each tetrahedral element, the sizes of the element matrices in (8)–(18) can be summarized in Table 2 for the traditional higher-order DGTD method. These element matrices need to be stored for each tetrahedral element. Therefore, the memory requirement is huge when a large-scale problem is analyzed.

In order to reduce the memory requirement of the DGTD method, the calculation methods of the element matrices in (9)–(18) are optimized. Note that the mass matrix $\left[\mathbf{M}^i\right]$ in (8) needs to be inversed before solving (6) and (7). The inverse matrix can share the same memory space with $\left[\mathbf{M}^i\right]$. Thus there is no need to optimize the calculation method of $\left[\mathbf{M}^i\right]$.

(1) The matrix $\left[\mathbf{C}^i\right]$ in (18) can be calculated as

$$\left[\mathbf{C}^i\right]_{kl} = \sigma \int_{V_i} \mathbf{N}_k^i \cdot \mathbf{N}_l^i dV$$
$$= \sigma \int_{V_i} (\sum_{m=1}^{3} N_{km}^i \nabla L_m^i) \cdot (\sum_{n=1}^{3} N_{ln}^i \nabla L_n^i) dV \tag{20}$$
$$= \sigma \sum_{m=1}^{3} \sum_{n=1}^{3} \nabla L_m^i \cdot \nabla L_n^i \int_{V_i} N_{km}^i N_{ln}^i dV$$

A coordinate transformation is introduced to simplify the calculation of the integral in (20). As shown in Fig. 3, a tetrahedral element in the global (x, y, z)-coordinate system is transformed into a normalized (L_1, L_2, L_3)-coordinate system. Each point (x, y, z) of the tetrahedral element in the global coordinate system can be transformed to a corresponding point (L_1, L_2, L_3) in the normalized coordinate system with the following relationship:

$$\begin{bmatrix} x \\ y \\ z \end{bmatrix} = \mathbf{J} \begin{bmatrix} L_1 \\ L_2 \\ L_3 \end{bmatrix} + \begin{bmatrix} x_4 \\ y_4 \\ z_4 \end{bmatrix} \tag{21}$$

$$\mathbf{J} = \begin{bmatrix} x_1 - x_4 & x_2 - x_4 & x_3 - x_4 \\ y_1 - y_4 & y_2 - y_4 & y_3 - y_4 \\ z_1 - z_4 & z_2 - z_4 & z_3 - z_4 \end{bmatrix} \tag{22}$$

$\mathbf{J}$ is the Jacobian matrix which only depends on the global coordinates (x, y, z).

Then the element integral in (20) can be calculated in the normalized coordinate system:

$$\int_{V_i} N_{km}^i N_{ln}^i dV = |\mathbf{J}| \int_{V_{ref}} N_{km}^i N_{ln}^i dV$$
$$= |\mathbf{J}| \int_{L_1=0}^{1} \int_{L_2=0}^{1-L_1} \int_{L_3=0}^{1-L_1-L_2} N_{km}^i N_{ln}^i dL_1 dL_2 dL_3 \tag{23}$$

Note that the integral in (23) only depends on the reference element in the normalized coordinate system. So this integral only needs to be calculated once for all the elements.
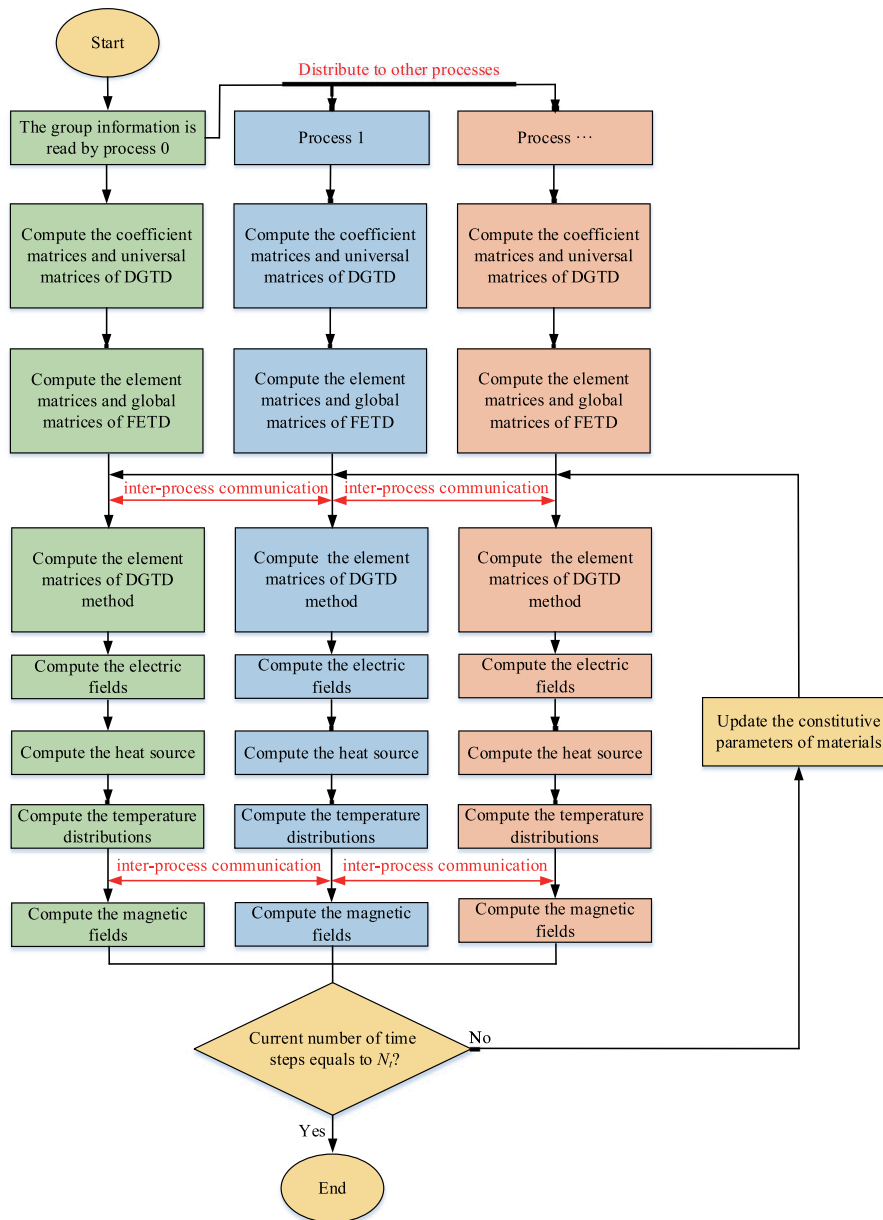
Fig. 4. Flow chart of the parallel algorithm.

Substituting (23) into (20), we can obtain

$$[\mathbf{C}^i]_{kl} = \sigma \sum_{m=1}^{3} \sum_{n=1}^{3} \left[\mathbf{C}^i_{coef}\right]_{mn} \left[\mathbf{C}^i_{universal}\right]_{mn}^{(kl)} \qquad (24)$$

where

$$\left[\mathbf{C}^i_{coef}\right]_{mn} = 6V_e \nabla L^i_m \cdot \nabla L^i_n \qquad (25)$$

$$\left[\mathbf{C}^i_{universal}\right]_{mn}^{(kl)} = \int_{L_1=0}^{1} \int_{L_2=0}^{1-L_1} \int_{L_3=0}^{1-L_1-L_2} N^i_{km} N^i_{ln} dL_1 dL_2 dL_3 \qquad (26)$$

where V_e is the volume of tetrahedron element. According to (24), we can store $\left[\mathbf{C}^i_{coef}\right]$ and $\left[\mathbf{C}^i_{universal}\right]^{(kl)}$ instead of store $[\mathbf{C}^i]$. Obviously, the matrix $\left[\mathbf{C}^i_{coef}\right]$ is element dependent with the size of 3×3 ($m = 1, 2, 3, n = 1, 2, 3$) for each tetrahedral element in the global coordinate system, while the matrix $\left[\mathbf{C}^i_{universal}\right]^{(kl)}$ is element independent with the size of 3×3×20×20 ($m = 1, 2, 3, n = 1, 2, 3, k = 1, \ldots, 20, l = 1, \ldots, 20$). Therefore,

$\left[\mathbf{C}^i_{universal}\right]^{(kl)}$ is calculated only once and its memory consumption is negligible. $\left[\mathbf{C}^i_{coef}\right]$ needs to be stored for each element but its size 3 × 3 is much smaller than $[\mathbf{C}^i]$ with the size of 20 × 20.

(2) Substituting (19) into (9), we can obtain

$$\nabla \times \mathbf{N}^i_l = \nabla \times \left(\sum_{m=1}^{3} N^i_{lm} \nabla L^i_m \right) = \sum_{m=1}^{3} S^i_{lm} \mathbf{b}^i_m \qquad (27)$$

where

$$\begin{cases} S^i_{l1} = \dfrac{\partial N^i_{l3}}{\partial L^i_2} - \dfrac{\partial N^i_{l2}}{\partial L^i_3} \\[2mm] S^i_{l2} = \dfrac{\partial N^i_{l1}}{\partial L^i_3} - \dfrac{\partial N^i_{l3}}{\partial L^i_1} \\[2mm] S^i_{l3} = \dfrac{\partial N^i_{l2}}{\partial L^i_1} - \dfrac{\partial N^i_{l1}}{\partial L^i_2} \end{cases} \qquad (28)$$

$$\begin{cases} \mathbf{b}_1^i = \nabla L_2^i \times \nabla L_3^i \\ \mathbf{b}_2^i = \nabla L_3^i \times \nabla L_1^i \\ \mathbf{b}_3^i = \nabla L_1^i \times \nabla L_2^i \end{cases} \tag{29}$$

Thus

$$[\mathbf{S}^i]_{kl} = \int_{V_i} (\sum_{m=1}^{3} N_{km}^i \nabla L_m^i) \cdot (\sum_{n=1}^{3} S_{ln}^i \mathbf{b}_n^i) dV \tag{30}$$

$$= \sum_{m=1}^{3} \sum_{n=1}^{3} \left[\mathbf{S}_{coef}^i\right]_{mn} \left[\mathbf{S}_{universal}^i\right]_{mn}^{(kl)}$$

where

$$\left[\mathbf{S}_{coef}^i\right]_{mn} = 6V_e \nabla L_m^i \cdot \mathbf{b}_n^i \tag{31}$$

$$\left[\mathbf{S}_{universal}^i\right]_{mn}^{(kl)} = \int_{L_1=0}^{1} \int_{L_2=0}^{1-L_1} \int_{L_3=0}^{1-L_1-L_2} N_{km}^i S_{ln}^i dL_1 dL_2 dL_3 \tag{32}$$

According to (30), we can store $\left[\mathbf{S}_{coef}^i\right]$ and $\left[\mathbf{S}_{universal}^i\right]^{(kl)}$ instead of store $[\mathbf{S}^i]$. The size of $\left[\mathbf{S}_{coef}^i\right]$ compared with $[\mathbf{S}^i]$ is given in Table 2.

(3) According to (14) and (16), the only difference between $\mathbf{F}_{ee}^{ii}$ and $\mathbf{F}_{hh}^{ii}$ is their coefficient, so their calculation methods are similar. Take $\mathbf{F}_{ee}^{ii}$ as an example, it can be calculated as

$$[\mathbf{F}_{ee}^{ii}]_{kl} = \frac{1}{Z^i + Z^j} \sum_{m=1}^{3} \sum_{n=1}^{3} \left[\mathbf{F}_{coef}^{ii}\right]_{mn}^{ee} \left[\mathbf{F}_{universal}^{ii}\right]_{mn}^{(kl)} \tag{33}$$

where

$$\left[\mathbf{F}_{coef}^{ii}\right]_{mn}^{ee} = 2A \nabla L_m^i \cdot \left(\hat{n} \times \hat{n} \times \nabla L_n^i\right) \tag{34}$$

$$\left[\mathbf{F}_{universal}^{ii}\right]_{mn}^{(kl)} = \int_{L_1=0}^{1} \int_{L_2=0}^{1-L_1} N_{km}^i N_{ln}^i dL_1 dL_2 \tag{35}$$

where A is the area of a face in the tetrahedron element.

(4) According to (10) and (12), the only difference between $\mathbf{F}_{eh}^{ii}$ and $\mathbf{F}_{he}^{ii}$ is their coefficients, so their calculation methods are similar. Take $\mathbf{F}_{eh}^{ii}$ as an example, it can be calculated as

$$[\mathbf{F}_{eh}^{ii}]_{kl} = \frac{Z^j}{Z^i + Z^j} \sum_{m=1}^{3} \sum_{n=1}^{3} \left[\mathbf{F}_{coef}^{ii}\right]_{mn}^{eh} \left[\mathbf{F}_{universal}^{ii}\right]_{mn}^{(kl)} \tag{36}$$

where

$$\left[\mathbf{F}_{coef}^{ii}\right]_{mn}^{eh} = 2A \nabla L_m^i \cdot \left(\hat{n} \times \nabla L_n^i\right) \tag{37}$$

Note that the universal matrix in $\mathbf{F}_{ee}^{ii}$, $\mathbf{F}_{hh}^{ii}$, $\mathbf{F}_{eh}^{ii}$ and $\mathbf{F}_{he}^{ii}$ are the same, namely $\left[\mathbf{F}_{universal}^{ii}\right]^{(kl)}$.

(5) According to (15) and (17), the calculation methods of $\mathbf{F}_{ee}^{ij}$ and $\mathbf{F}_{hh}^{ij}$ are similar. Take $\mathbf{F}_{ee}^{ij}$ as an example, it can be calculated as

$$[\mathbf{F}_{ee}^{ij}]_{kl} = \frac{1}{Z^i + Z^j} \sum_{m=1}^{3} \sum_{n=1}^{3} \left[\mathbf{F}_{coef}^{ij}\right]_{mn}^{ee} \left[\mathbf{F}_{universal}^{ij}\right]_{mn}^{(kl)} \tag{38}$$

where

$$\left[\mathbf{F}_{coef}^{ij}\right]_{mn}^{ee} = 2A \nabla L_m^i \cdot \left(\hat{n} \times \hat{n} \times \nabla L_n^j\right) \tag{39}$$

$$\left[\mathbf{F}_{universal}^{ij}\right]_{mn}^{(kl)} = \int_{L_1=0}^{1} \int_{L_2=0}^{1-L_1} N_{km}^i N_{ln}^j dL_1 dL_2 \tag{40}$$

(6) According to (11) and (13), the calculation methods of $\mathbf{F}_{eh}^{ij}$ and $\mathbf{F}_{he}^{ij}$ are similar. Take $\mathbf{F}_{eh}^{ij}$ as an example, it can be calculated as

$$[\mathbf{F}_{eh}^{ij}]_{kl} = \frac{Z^j}{Z^i + Z^j} \sum_{m=1}^{3} \sum_{n=1}^{3} \left[\mathbf{F}_{coef}^{ij}\right]_{mn}^{eh} \left[\mathbf{F}_{universal}^{ij}\right]_{mn}^{(kl)} \tag{41}$$

where

$$\left[\mathbf{F}_{coef}^{ij}\right]_{mn}^{eh} = 2A \nabla L_m^i \cdot \left(\hat{n} \times \nabla L_n^j\right) \tag{42}$$

Table 2
Comparison of the memory requirements between the traditional higher-order DGTD method and the proposed method.

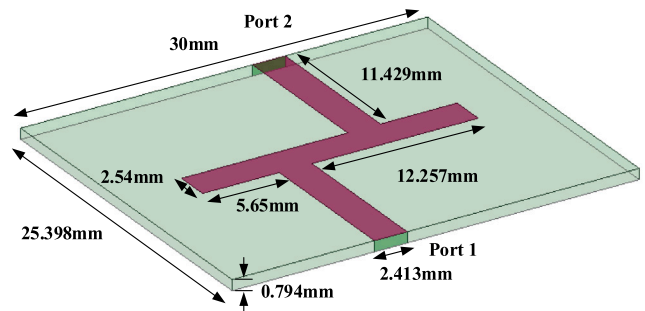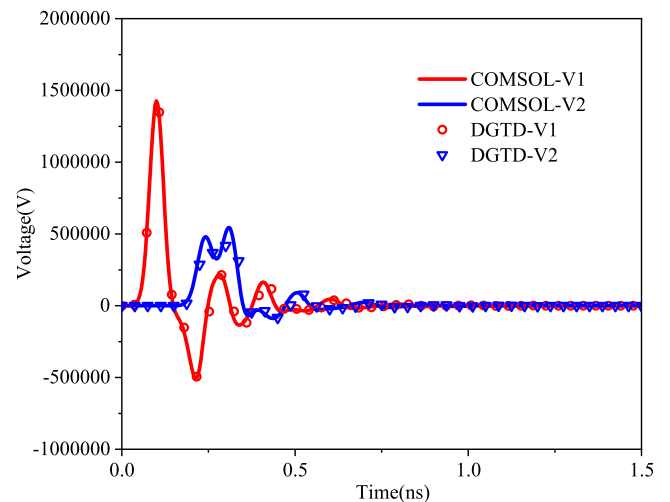| Matrices	Traditional method	Matrices	Proposed method
$[\mathbf{M}^i]$	20×20	$[\mathbf{M}^i]$	20×20
$[\mathbf{C}^i]$	20×20	$[\mathbf{C}_{coef}^i]$	3×3
$[\mathbf{S}^i]$	20×20	$[\mathbf{S}_{coef}^i]$	3×3
$[\mathbf{F}_{ee}^{ii}]$	20×20	$[\mathbf{F}_{coef}^{ii}]^{ee,hh}$	$3 \times 3 \times 4$
$[\mathbf{F}_{hh}^{ii}]$	20×20		
$[\mathbf{F}_{eh}^{ii}]$	20×20	$[\mathbf{F}_{coef}^{ii}]^{eh,he}$	$3 \times 3 \times 4$
$[\mathbf{F}_{he}^{ii}]$	20×20		
$[\mathbf{F}_{ee,hh}^{ij}]$	$20 \times 20 \times 4$	$[\mathbf{F}_{coef}^{ij}]^{ee,hh}$	$3 \times 3 \times 4$
$[\mathbf{F}_{eh,he}^{ij}]$	$20 \times 20 \times 4$	$[\mathbf{F}_{coef}^{ij}]^{eh,he}$	$3 \times 3 \times 4$

Fig. 5. A microstrip low-pass filter.

Fig. 6. Port voltages V1 and V2 obtained by the proposed method and COMSOL based on single electromagnetic simulation.

Note that the universal matrix in $\mathbf{F}_{ee}^{ij}$, $\mathbf{F}_{hh}^{ij}$, $\mathbf{F}_{eh}^{ij}$ and $\mathbf{F}_{he}^{ij}$ are the same, namely $\left[\mathbf{F}_{universal}^{ij}\right]^{(kl)}$.

The sizes of the element matrices in (8)–(18) in traditional computation method and the sizes of the corresponding matrices which primarily need to be stored in the proposed method are compared and summarized in Table 2. Apparently the sizes of the matrices to be stored in the proposed method is much smaller than the traditional method, resulting in remarkable memory saving.
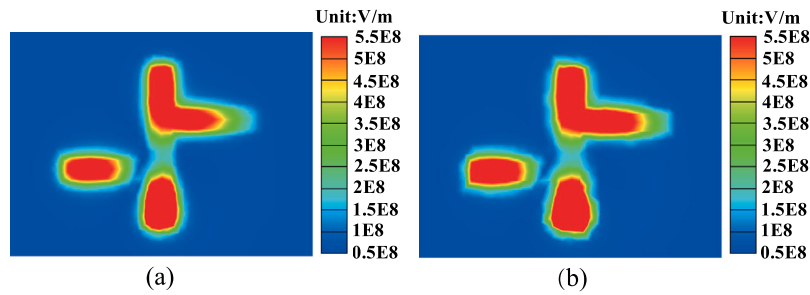
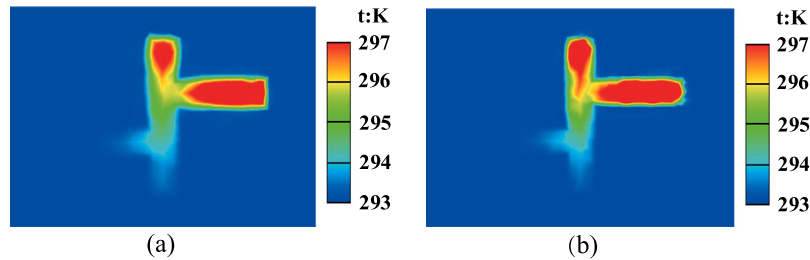**Fig. 7.** Electric field distributions at $t = 0.5$ ns: (a) Proposed. (b) COMSOL.

Fig. 8. Temperature distributions at $t = 0.5$ ns: (a) Proposed. (b) COMSOL.

2.3. Parallel strategies

The electromagnetic-thermal co-simulation algorithm is parallelized based on MPI technique. Fig. 4 shows the parallel algorithm flow chart. Firstly, the tetrahedral meshes are divided into different groups by using the METIS software [19]. The group information for all the tetrahedral elements is recorded in a mesh file, which is read by the process 0 and distributed to other processes. In the following, each process will only carry out computations related to its own meshes.

Then the inverse matrix of $\left[\mathbf{M}^i\right]$ in (8), the coefficient matrices and universal matrices for the matrices in (9)–(18) of DGTD method are computed and stored for the electromagnetic simulation. The element matrices and the global matrices of FETD method corresponding to each process are computed for the thermal simulation.

After above matrices are computed, the matrix equations for the electromagnetic simulation and thermal simulation are solved in a marching-on-in-time manner. The matrix Eq. (6) is solved element by element to obtain the electric fields, during which the matrices in (9)–(18) are computed based on the coefficient matrices and universal matrices. Then the heat source for the thermal simulation is calculated and the temperature distributions are obtained by solving the matrix equation of FETD method. At last, the magnetic fields are calculated by solving (7). After the electric fields, temperature distributions and magnetic fields are computed, the program will end if the current number of time steps equals to the specified number of time steps N_t. Otherwise, the constitutive parameters of materials are updated. The matrix equations for electromagnetic and thermal simulation are solved for the next time step.

3. Numerical results

In this section, two numerical examples are given to demonstrate the performance of the proposed method. The electromagnetic properties of the microstrip filters are analyzed with a single electromagnetic simulation and the electromagnetic-thermal co-simulation. All the simulations are carried out using 16 processes parallel computation on a workstation with Intel Xeon Gold 6248R CPU with 48 cores and 1 TB RAM.
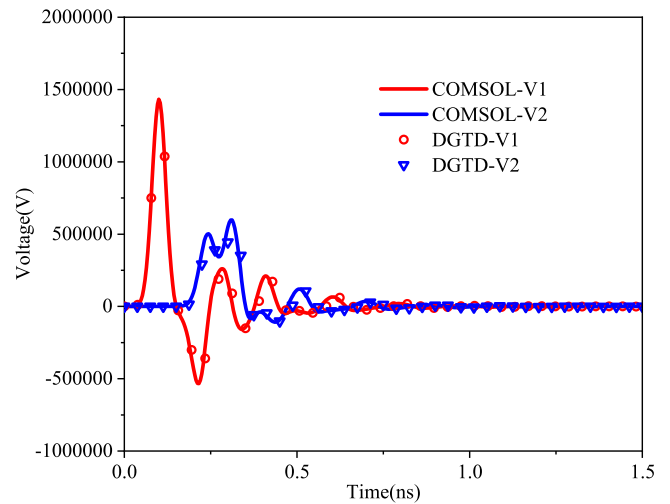

Fig. 9. Port voltages V1 and V2 obtained by the proposed method and COMSOL based on electromagnetic-thermal co-simulation.

3.1. Electromagnetic-thermal co-simulation of a microstrip low-pass filter

As illustrated in Fig. 5, a microstrip low-pass filter resides 0.794 mm above the ground plane. The length and width of the ground plane are 30 mm and 25.398 mm, respectively. The relative dielectric constant and conductivity of the substrate are 2.2 and 0.1 S/m, respectively. Port 1 and port 2 are two lumped ports. In order to model the scenario of the injection of high power pulse, a Gaussian pulse source is utilized as the excitation at port 1. The expression for the Gaussian pulse is as follows:

$$V_s(t) = V_0 \exp\left[-\frac{4\pi(t - t_0)^2}{\tau^2}\right] \tag{43}$$

where $V_0 = 3 \times 10^6$ V and $t_0 = \tau = 0.1$ ns. Port 2 is connected with a 50 Ω resistor. The perfectly matched layer (PML) is used to truncate the computational domain. The whole geometry is meshed into 34 756

Table 3

Memory usage and time consumption of the traditional higher-order DGTD method and the proposed method.

Model	Elements	Traditional method		Proposed method		Memory usage ratio	Time consumption ratio
		Memory (MB)	Time (s)	Memory (MB)	Time (s)		
Low-pass filter	34 756	1635.7	4652	193.8	7817	0.118	1.68
Band-stop filter	34 607	1628.6	4744	193.3	7753	0.119	1.63
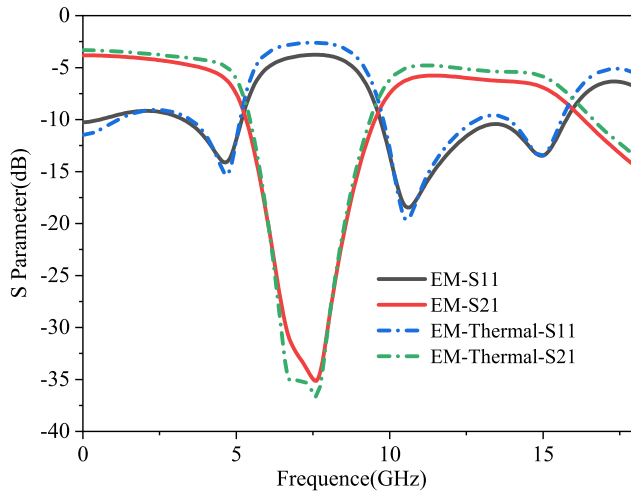
Fig. 10. S11 and S21 curves of the microstrip low-pass filter based on single electromagnetic simulation and electromagnetic-thermal co-simulation.

Fig. 11. A microstrip band-stop filter.

Fig. 12. The voltages of port a corresponding to ambient temperatures of 253.15 K, 293.15 K and 353.15 K.

tetrahedral elements. The total simulation time is set to be 1.5 ns. The total number of time steps is 50,000.

Firstly, the single electromagnetic simulation is carried out with our own code and the COMSOL software. As shown in Fig. 6, the port voltages V1 and V2 obtained by the proposed method are in good agreement with COMSOL. Then the electromagnetic-thermal co-simulation of the microstrip low-pass filter is conducted. The thermal parameters are $\rho = 2330$ kg/m^3, $C_\rho = 704$ J/(kg K), $\alpha = 0.2$ (1/K), and $\kappa = 30$ W/(m K). In the thermal simulation, it is assumed that all boundary surfaces of the model are convective boundary conditions with the heat transfer coefficient $h = 5$ W/(m^2 K). The ambient temperature and initial temperature are 293.15 K. Figs. 7 and 8 present the electric field and temperature distributions on the plane of z = 0 mm at 0.5 ns obtained by the proposed method and COMSOL. Good agreement can be observed. The port voltages are shown in Fig. 9. The results obtained by our proposed method are also in good agreement with COMSOL.

As shown in Fig. 10, the S11 and S21 curves of the filter are computed based on the port voltages obtained by the single electromagnetic simulation and electromagnetic-thermal co-simulation. Significant differences between the electromagnetic simulation and electromagnetic-thermal co-simulation can be observed, which clearly demonstrates the temperature-drift effect of microstrip filters and supports the necessity of the electromagnetic-thermal co-simulation. As shown in Table 3, if the traditional electromagnetic-thermal co-simulation method without the memory reduction technique is adopted for this problem, the memory consumption is 1635.7 MB. In contrast, if the proposed method is utilized, the memory consumption is 193.8 MB, which is only 11.8% of the traditional method. The memory reduction of the proposed method is at the expense of computation time. As we can observe from Table 3, the CPU time of the proposed method is 1.68 times of the traditional method.

3.2. Electromagnetic-thermal co-simulation of a microstrip band-stop filter

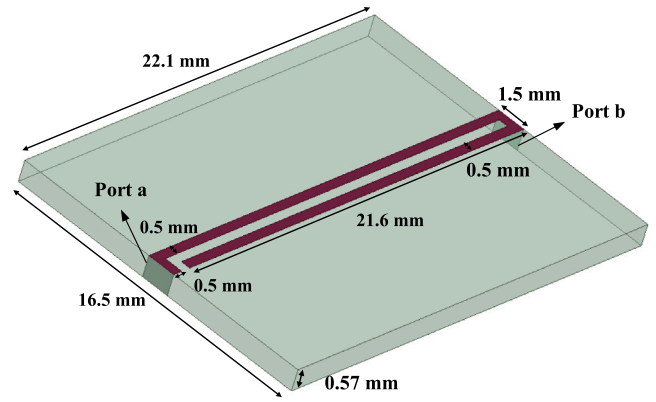In the second example, a microstrip band-stop filter working at different ambient temperatures is simulated to investigate the influence of ambient temperature on the electroma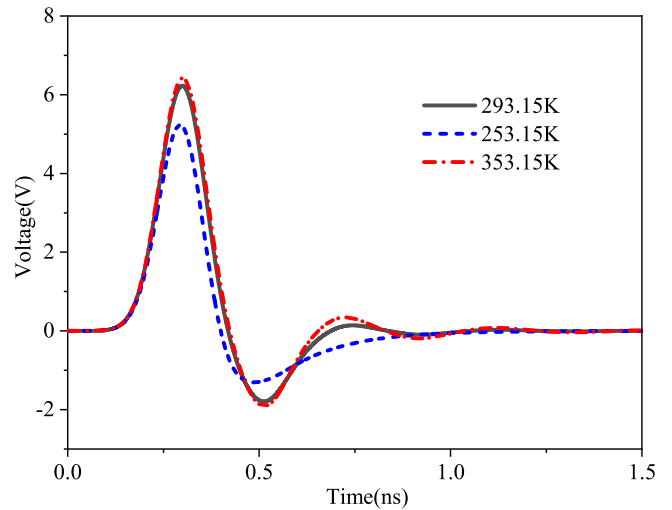gnetic property of microstrip filter. As illustrated in Fig. 11, the microstrip band-stop filter resides 0.57 mm above the ground plane. The length and width of the ground plane are 22.1 mm and 16.5 mm, respectively. The relative dielectric constant and conductivity of the substrate are 2 and 0.1 S/m, respectively. The thermal parameters are the same as the first example, except for $\alpha = 0.02$ (1/K). Port a and port b are two lumped ports. The port a is driven by a Gaussian pulse source, its expression is shown in (43), where $V_0 = 10$ V and $t_0 = \tau = 0.3$ ns. Port b is connected with a 50 Ω resistor. The whole structure is meshed into 34 607 tetrahedral elements. The total simulation time is set to be 1.5 ns. The total number of time steps is 50,000.

Electromagnetic-thermal co-simulations of the microstrip band-stop filter working at ambient temperatures of 253.15 K, 293.15 K and 353.15 K are carried out by the proposed method. As shown in Figs. 12 and 13, the port voltages change significantly when the ambient temperatures deviate from the room temperature of 293.15 K. The electric distributions on the plane of z = 0 mm at 0.5 ns are shown in Fig. 14.

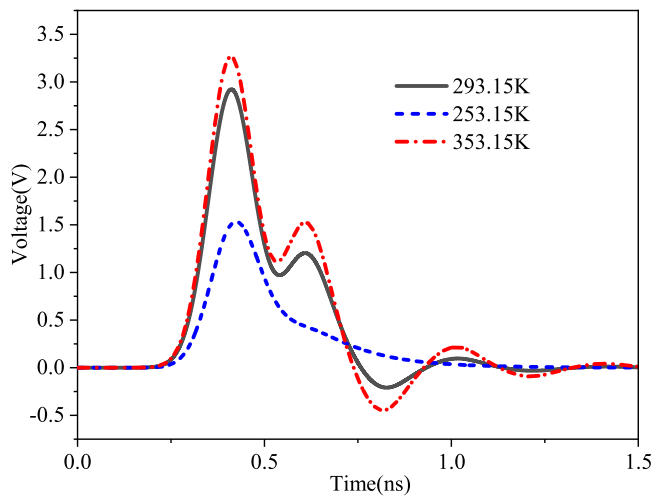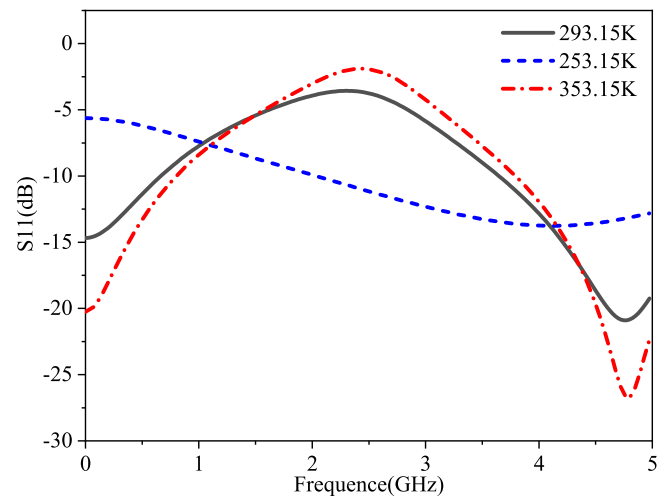**Fig. 13.** The voltages of port b corresponding to ambient temperatures of 253.15 K, 293.15 K and 353.15 K.
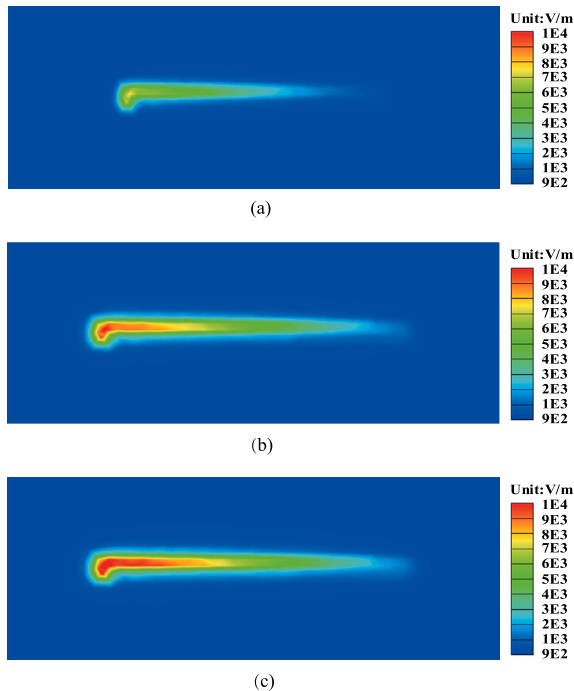

Fig. 14. Electric field distributions at t = 0.3 ns corresponding to different ambient temperatures: (a) 253.15 K, (b) 293.15 K, (c) 353.15 K.

Fig. 15. Comparison of S11 under different ambient temperatures.

Fig. 16. Comparison of S21 under different ambient temperatures.

It can be observed that the electric distributions corresponding to different ambient temperatures are obviously different.

As shown in Figs. 15 and 16, the S11 and S21 curves of the microstrip band-stop filter are computed based on the port voltages in Figs. 12 and 13. Similar with the first numerical example, significant temperature-drift effect can be observed. As shown in Table 3, if the traditional electromagnetic-thermal co-simulation method without the memory reduction technique is adopted for this problem, the memory consumption is 1628.6 MB. In contrast, if the proposed method is utilized, the memory consumption is 193.3 MB, which is only 11.9% of the traditional method. The CPU time of the proposed method is 1.63 times of the traditional method.
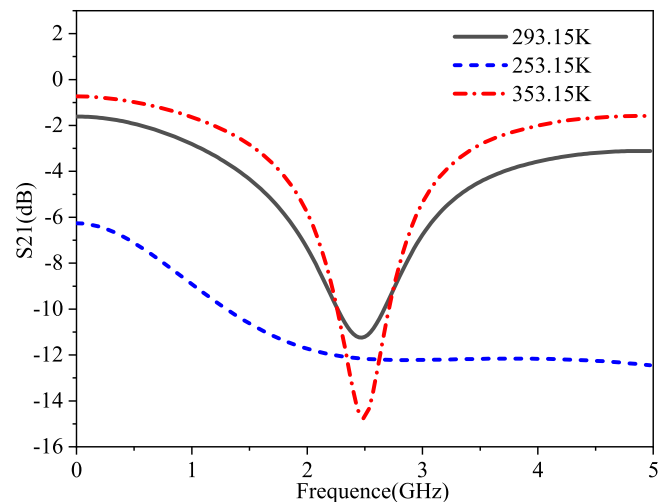
4. Conclusion

A transient electromagnetic-thermal co-simulation method is proposed for the analyze of temperature-drift effect of microstrip filters. The DGTD method with the higher-order hierarchical vector basis functions and the memory reduction technique is adopted for the electromagnetic simulation. The FETD method is utilized for the thermal simulation. Large-scale parallel technique is used to accelerate the simulation process. Numerical results show that the proposed method can efficiently reduce the memory requirement of the electromagnetic-thermal co-simulation method, which allows for an effective and powerful tool for the temperature-drift effect analyze of microstrip filters in complicated engineering applications.

Declaration of competing interest

The authors declare that they have no known competing financial interests or personal relationships that could have appeared to influence the work reported in this paper.

Data availability

No data was used for the research described in the article

Acknowledgments

References

[1] Hong JS. Microstrip filters for rf/microwave applications. 2nd ed.. John Wiley & Sons, Inc; 2011.

[2] Haala J, Wiesbeck W. Modeling microwave and hybrid heating processes including heat radiation effects. IEEE Trans Electromagn Compat 2002;50(5):1346–54.

[3] Torres F, Jecko B. Complete FDTD analysis of microwave heating processes in frequency dependent and temperature-dependent media. IEEE Trans Microw Theory Tech 1997;45(1):108–17.

[4] Ma L, Paul DL. Experimental validation of a combined electromagnetic and thermal FDTD model of a microwave heating process. IEEE Trans Microw Theory Tech 1995;1(43):2565–72.

[5] Li N, Mao JF, Zhao WS, Tang M, Chen WC, Yin WY. Electrothermal cosimulation of 3-D carbon-based heterogeneous interconnects. IEEE Trans Compon Packag Manuf Tech 2016;6(4):1–9.

[6] Lu TJ, Jin JM. Transient electrical-thermal analysis of 3-D power distribution network with FETI-enabled parallel computing. IEEE Trans Compon Packag Manuf Tech 2014;4(10):1684–95.

[7] Lu TJ, Jin JM. Electrical-thermal co-simulation for DCIR-drop analysis of large-scale power delivery. IEEE Trans Compon Packag Manuf Tech 2014;4(2):323–31.

[8] Lu TJ, Jin JM. Thermal-aware high-frequency characterization of large-scale through-Silicon-via structures. IEEE Trans Compon Packag Manuf Tech 2014;4(6):1015–25.

[9] Lu TJ, Jin JM. Electrical-thermal co-simulation for analysis of high-power RF/microwave components. IEEE Trans Electromagn Compat 2017;59(1):93–102.

[10] Zhang HH, Sha WEI, et al. Electromagnetic-thermal analysis of human head exposed to cell phones with the consideration of radiative cooling. IEEE Antennas Wirel Propag Lett 2018;17(9):1584–7.

[11] Dong Y, Tang M, Li P, Mao J. Transient electromagnetic-thermal simulation of dispersive media using DGTD method. IEEE Trans Electromagn Compat 2019;61(4):1305–13.

[12] Chen PY, Zhang HH, Sha EIW, Ding DZ. Transient electromagnetic-thermal cosimulation based on DGTD method. In: 2019 international applied computational electromagnetics society symposium-China. ACES, 2019, p. 1–2.

[13] Zhang HH, Jiang LJ, Yao HM, Zhang Y. Transient heterogeneous electromagnetic simulation with DGTD and behavioral macromodel. IEEE Trans Electromagn Compat 2017;59(4):1152–60.

[14] Zhang HH, Sha WEI, Huang ZX, et al. Flexible and accurate simulation of radiation cooling with FETD method. Sci Rep 2018;8(1).

[15] Li P, Dong Y, Tang M, Mao J, Jiang LJ, Bagci H. Transient thermal analysis of 3-D integrated circuits packages by the DGTD method. IEEE Trans Compon Packag Manuf Tech 2017;7(6):862–71.

[16] Hesthaven JS, Warburton T. Nodal discontinuous galerkin methods. Berlin: Springer; 2008.

[17] Webb J. Hierarchal vector basis functions of arbitrary order for triangular and tetrahedral finite elements. IEEE Trans Antennas Propag 1999;47(8):1244–53.

[18] Andersen LS, Volakis JL. Hierarchical tangential vector finite elements for tetrahedra. IEEE Microw Guided Wave Lett 1998;8(3):127–9.

[19] Pospisek T, Konecny D. METIS. Springer Berlin Heidelberg; 2010.